Plasma nitriding of 410S ferritic/martensitic stainless steel: microstructure, wear and corrosion properties

Luiz Bernardo Varela Jimenez [1] (iD)
Milena Tosti Umemura [2] (iD)
José Wilmar Calderón-Hernández [3] (iD)
Rodrigo Magnabosco [4] (iD)
Carlos Eduardo Pinedo [5*] (iD)
André Paulo Tschiptschin [3] (iD)

Abstract

In this work, plasma nitriding treatments were performed on ferritic/martensitic stainless steel type 410S at 400 ºC (Low-temperature Plasma Nitriding - LTPN) and 530 ºC (Conventional Plasma Nitriding - CPN). The treatments were carried out under a 75% N_2-25% H_2 gas mixture for 20 hours. After LTPN, a layer composed of expanded ferrite/martensite with a minor fraction of iron nitrides was obtained. In CPN, the nitrided surface consists of an outermost compound layer 15 μm thick followed by a diffusion zone with a depth of 170 μm. After both, CPN and LTPN nitriding treatments, the surface hardness increases more than four times compared to the original hardness of the non-nitrided steel and results in a flat-type transverse hardening profile for CPN and a diffuse-type profile for LTPN. The friction coefficients in the CPN and LTPN conditions, evaluated by the progressive linear scratching test, are lower than the condition without nitriding. The wear rate after nitriding is half that found for the non-nitriding condition. The corrosion resistance evaluated by immersion test in an aqueous solution with 3% $FeCl_3$ for 88 hours shows that the behavior after LTPN is the same as in the non-nitrided condition, while for the CPN, the mass loss is higher and, therefore, the corrosion resistance is smaller than that observed for the LTPN. The precipitation of chromium nitrides during CPM nitriding leads to chromium depletion in the metal matrix. The results show the feasibility of promoting surface hardening of type 410S stainless steel by nitriding at low temperatures and improving the tribological properties without compromising corrosion resistance.

Keywords: Plasma nitriding; Stainless steel; Hardening; Wear; Corrosion.

Nitretação sob plasma do aço inoxidável ferrítico/martensítico 410S: microestrutura e propriedades em desgaste e corrosão

Resumo

Neste trabalho foram realizados tratamentos sob plasma no aço inoxidável ferrítico/martensítico tipo 410S a baixa temperatura 400 ºC (LTPN) e na temperatura convencional de 530 ºC (CPN). Os tratamentos foram realizados sob uma mistura gasosa composta de 75% N_2-25% H_2 por 20 horas. Após a LTPN foi obtida uma camada composta por ferrita/martensita expandida com uma fração minoritária de nitretos de ferro. Na CPN a superfície nitretada é constituída da camada de compostos com 15 μm de espessura seguida pela zona de difusão com 170 μm de profundidade. Após os tratamentos de nitretação CPN e LTPN a dureza superficial aumenta até mais de 4 vezes a dureza original do aço não nitretado e resulta em um perfil de endurecimento transversal do tipo plano para a CPN e do tipo difuso para a LTPN. Os coeficientes de atrito nas condições CPN e LTPN, avaliados por ensaio de riscamento linear progressivo, são inferiores à condição sem nitretação. A taxa de desgaste após a nitretação é a metade da encontrada para a condição sem nitretação. A resistência à corrosão avaliada por ensaio de imersão em uma solução aquosa com 3% $FeCl_3$ por 88 horas mostra que o comportamento após a LTPN é igual ao da condição não nitretada, enquanto para a CPN a perda de massa é superior e, portanto, menor que a observada para a LTPN. A precipitação de nitretos de cromo, durante a nitretação CPM, conduz ao empobrecimento de cromo na matriz metálica. Os resultados mostram que é possível promover o endurecimento superficial do aço tipo 410S por nitretação a baixa temperatura com melhoria nas propriedades tribológicas sem comprometimento da resistência à corrosão.

Palavras-chave: Nitretação sob plasma; Aço inoxidável; Endurecimento; Desgaste; Corrosão.

[1] Department of Engineering Physics, Polytechnique Montréal, Québec, Canada.
[2] Institut National des Sciences Appliquées de Lyon, INSA Lyon, Villeurbanne, France.
[3] Departamento de Engenharia Metalúrgica e de Materiais, Universidade de São Paulo, São Paulo, SP, Brasil.
[4] Departamento de Engenharia de Materiais, Centro Universitário FEI, São Bernardo do Campo, SP, Brasil.
[5] Heat Tech Technology for Heat Treatment and Surface Engineering Ltd, Mogi das Cruzes, SP, Brasil.

*Corresponding author: pinedo@heattech.com.br

1 Introduction

Stainless steels have been employed in the chemical, petrochemical, pharmaceutical, biomedical, and food industries, where corrosion resistance and biological compatibility are essential. However, the hardness of such steels is low, and wear resistance is not adequate for some service requirements. When in contact with abrasive particles, these materials undergo two-body and three-body wear under high contact stresses, being scratched or indented, impairing performance. Plasma diffusion treatments have been studied to increase stainless steel's surface hardness and wear resistance. It is well known that stainless steel is very sensitive to surface diffusion hardening temperatures. Nitriding at temperatures higher than 480 °C (CPN) leads to intense chromium and iron nitrides precipitation in the diffusion zone, increasing the surface hardness but severely impairing corrosion resistance [1-4].

On the other hand, low-temperature plasma nitriding (LTPN) carried out at temperatures below 430 °C can increase surface hardness by up to eight times, leading to more wear-resistant materials. At the same time, LTPN contributes to preventing chromium nitrides precipitation and chromium depletion in the matrix, granting corrosion resistance as good as that of non-nitrided conditions. This strong hardening effect is due to introducing a large amount of interstitially dissolved nitrogen in solid solution. As a consequence, metastable nitrogen supersaturated phases may form: expanded austenite (γ_N) [5-9], expanded martensite (α'_N) [10-14], and expanded ferrite (α_N) [15-18].

The diffraction patterns of low-temperature nitrided austenitic stainless steels show broader and shifted to the left diffraction peaks due to differential surface layer expansion and build-up of compressive stresses in the surface layer. Both lattice distortion by nitrogen supersaturation and compressive stresses increase the hardness of the surface layer to values between 10 and 14 GPa. Expanded austenite (γ_N), expanded ferrite (α_N), and expanded martensite (α'_N) have been characterized by X-ray diffraction (XRD) and selected area electron diffraction (SAED) using transmission electron microscopy. Most of the published papers describe these phases as being FCC or BCC metastable phases, containing colossal amounts of nitrogen in solid solution, (15 at% N to 40 at% N) or (4 wt% N to 14 wt% N), without precipitation or at least with minor precipitation of compounds owing to the strong Cr-N bond (high negative enthalpy) and very low diffusivity of chromium (high activation energy) [19].

This work presents a study on Conventional Plasma Nitriding (CPN) at 530°C and Low-Temperature Plasma Nitriding (LTPN) at 400 °C of 410S ferritic/martensitic stainless steel and reports the obtained microstructures, the surface hardening, wear and corrosion resistance.

2 Experimental details

2.1 Material and plasma nitriding

The chemical composition of the AISI 410S ferritic-martensitic stainless steel is shown in Table 1.

The 410S stainless steel was supplied in the air-cooled solution-treated condition with a ferritic-martensitic microstructure and a 310 HV hardness. 24 mm × 19 mm × 3 mm specimens were cut from the AISI 410S sheet and wet ground with SiC paper from 240 down to 1200 and diamond polished to the final 1 μm surface finishing.

Plasma nitriding treatments were carried out on a Rübig hot wall Pulsed-DC reactor. The cycle was started by purging the atmosphere up to 0.10 mbar and heating up to 380 °C. The specimens were plasma sputtered under a 100% hydrogen atmosphere at 380 °C for 1.5 hours, under 600 V and 1.0 mbar pressure, to remove the Cr_2O_3 passive film and activate the surface. After sputtering, plasma nitriding was carried out at 400 °C (LTPN) and 530°C (CPN) for 20 h with a gas mixture of 75% N_2:25% H_2 under a 470V voltage and 2.5 mbar pressure. After nitriding, samples were cooled down to room temperature under vacuum.

2.2 Microstructure and hardening characterization

The cross-sections of the as-received and nitrided samples were polished and etched for microstructure observation. Polishing was carried out using diamond suspension down to 1 μm. The polished surfaces were etched with Vilella's and Nital 4% reagents. The microstructures of the nitrided and non-nitrided specimens were analyzed by Light Optical Microscopy (LOM). The phases in the nitrided case were identified by X-Ray Diffraction (XRD) in a Phillips diffractometer using CuKα radiation, λ = 0.1542 nm, with a conventional θ/2θ Bragg-Brentano symmetric geometry, in the 2θ range from 30° to 90°.

Surface hardness and transverse microhardness profiles were assessed in a Shimadzu HMV-2 microhardness tester using 50 gf and 25 gf loads. The microhardness profile was measured from the surface to the core using a 25 gf load and a dwelling time of 15 s. The nitrided case depth was determined using the nitriding hardness depth (NHT) DIN 50190-3 standard.

Nanoindentation tests were conducted in a Hysitron – TI 950 Triboindenter, using a Berkovich three-faceted diamond

Table 1. Chemical composition of the AISI 410S stainless steel (wt. %)

C	Cr	Ni	Mn	Si	P	S	Fe
0.04	11.10	0.32	0.57	0.66	0.026	0.002	Bal.

pyramid indenter. The nanoindentation measurements were carried out on the surface of the nitrided and non-nitrided specimens using a loading/unloading rate of 1400 µN/s up to a peak load of 7000 µN. The peak load was held constant for a period of 5 s. The hardness (H) and Young modulus (E) were determined according to the procedure of Oliver and Pharr [20]. The H/E ratio and the elastic recovery parameter ($W_e = 1 - h_f/h_{max}$) were also determined. The energy dissipation coefficient (K_d) was calculated as the ratio of the plastic to the total deformation energy (E_p/E_t), as proposed by Recco et al. [21]. The plastic deformation energy (E_p) was determined by the difference between the area under loading, called the total energy (E_t), and unloading indentation curves, called elastic deformation energy (E_e). These energies were measured by integrating a function of the loading and unloading curves. A second-degree polynomial function approximated the curves.

2.3 Scratch and microabrasion tests

Scratch tests were conducted using a Rockwell C indenter with a spherical tip radius of 200 µm. Scratches, 5 mm in length, were made employing a linearly-increased normal force from a preload of 1 N up to a load of 50 N at a constant speed of 0.16 mm/s on the surfaces of the nitrided and non-nitrided specimens. During the scratch tests, the friction coefficients were measured from the ratio between lateral and normal force. Critical loads (L_C) for damaging the nitrided layers were determined by measuring the distance at which the first failure appeared along the scratch track and under a corresponding value of the normal load. The failure identification and distance measurements were carried out using a FEG-SEM.

Microabrasion testing was carried out to simulate the wear behavior of the plasma nitrided samples. A commercial Calowear - Anton Paar microabrasion tester with a 25.4 mm diameter free ball was used for the microabrasion tests. The ball rotation speed was n = 37.6 rpm, and the abrasive slurry (25%SiC + 75% distilled water, in volume) was continuously agitated and fed to the specimen-ball contact at a rate of one drop every 2 s. Tests were performed with six different sliding distances (S), $S_1 = 10$ m, $S_2 = 16$ m, $S_3 = 25$ m, $S_4 = 40$ m, $S_5 = 63$ m, and $S_6 = 100$ m, under an applied normal force of 0.4 N. The steel ball was pre-conditioned in an abrasive slurry prepared with black silicon carbide abrasive particles and distilled water for 30 min. Steady-state condition wear coefficients were calculated after 30 min of a running-in period before the ball-cratering wear tests. SEM images of the wear scars were acquired to understand the wear mechanisms operating at the tribosurfaces. A non-contact profilometry evaluation was done in a CCI-MP device from Taylor Hobson to determine the profile of the wear crater, thus allowing the calculation of the total worn volume. The non-contact profilometry evaluation allowed measuring the depth of the wear craters "h", which was used in Equation 1 to calculate the wear volumes [22]:

$$V \approx \pi R h^2 \qquad (1)$$

For h << R, "h" being the depth of the wear crater, and "R" is the radius of the ball.

2.4 Corrosion test

Corrosion tests were conducted by immersing the non-nitrided and nitrided samples in a 3% $FeCl_3$ solution for 88 h at room temperature. During the immersion test, the samples were removed from the solution at specific time intervals to examine the kinetics of dissolution; the specimens were cleaned with water, dried with warm air, and weighed on a scale to an accuracy of 0.0001 g to determine the weight loss. Three tests were performed for each condition. An examination of the corroded surfaces complemented the weight loss results by Stereomicroscopy.

3 Results

3.1 X-ray diffraction results

Figure 1 shows the diffraction patterns of the studied specimens. For the non-nitrided condition, three regular diffraction peaks with 2θ angles of 44.5, 64.5, and 82.1° can be assigned to bcc α-Fe, with a calculated lattice parameter
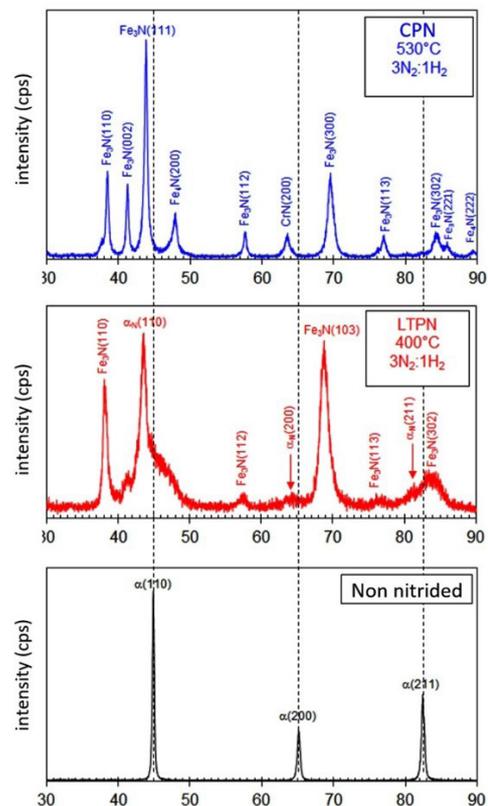

Figure 1. DRX diffraction patterns.

of 0.2866 nm, close 0.287 from the reference value (ICCD 00-001-1262). After LTPN, the surface of the nitrided 410S steel contained ε-Fe$_3$N iron nitride (ICCD 00-049- 1663) and small quantities of γ'-Fe$_4$N nitride (ICCD 00-003-0958). Three shifted to the left bcc peaks, located at 43.5°, 63.9°, and 81.8°, indicate the presence of nitrogen supersaturated expanded ferrite/martensite α$_N$/α'$_N$, in agreement with published works in the literature [23-26]. The lattice parameter calculated for the expanded ferrite/martensite peak at 43.5° corresponds to 0.2946 nm. Comparing this value to the α-Fe (110) peak of the non-nitrided alloy, located at 44.6°, one can see that plasma nitriding increased the martensite lattice parameter, shifting the α-Fe (110) peak to lower angles. It is worth noting that part of the lattice expansion is due to the development of compressive stresses in the nitrided layer [27]. However, an approximation of the nitrogen content in the expanded ferrite/martensite phase, not considering the effect of the compressive stresses, can be estimated using the calculated ferrite/martensite lattice parameters of the 410S stainless steel before and after LTPN using Cheng and Mittemeijer in Equation 2 [28]:

$$a_{\alpha N} = a_\alpha + a_\alpha\, 0.0092\ (at.\%\ N) \qquad (2)$$

Obtaining an atomic percentage of dissolved nitrogen for LTPN of 2.86 at% N in the supersaturated martensite.

The X-ray diffraction pattern of the conventional nitrided surface (CPN) shows ε-Fe$_3$N and γ'-Fe$_4$N iron nitrides peaks and CrN (ICCD 00-011-0065) phase, located at 43.5° and 63.9°, respectively. No peaks from the ferritic/martensite 410S stainless steel substrate appeared in the X-ray diffraction pattern, suggesting that the X-ray used for phase analysis did not cross the substrate, and such peaks refer only to the compound layer position.

3.2 Microstructure and hardening

Figure 2 shows the microstructure of the as-received 410S stainless steel containing 35% ferrite and 65% martensite.
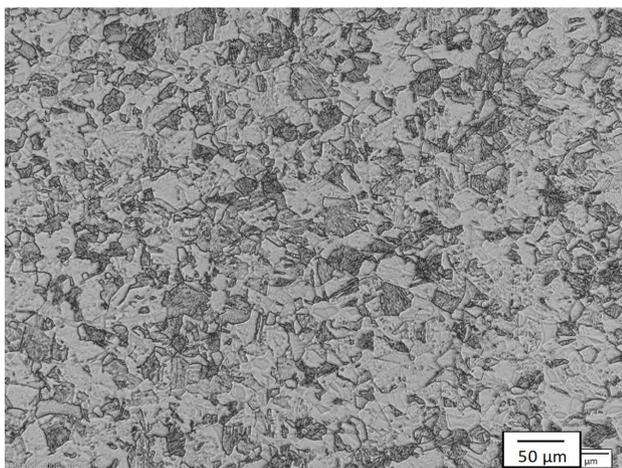
The different plasma nitriding temperatures led to different surface finishes compared to the initially polished starting condition. Figure 3 shows that the change of surface finish after LTPN is negligible, while CPN promotes an intense darkening of the polished surface and compromises the initial finishing condition. These results show an important advantage of LTPN in preserving the surface finishing of stainless steel parts destined for nitriding. Figure 4 shows the surfaces seen using LOM before and after nitriding. After LTPN, Figure 4(b), the steel grain structure is revealed, compared to the as-polished starting condition, due to the stress relief effect caused by the deformation caused by high nitrogen supersaturation and the formation of expanded ferrite/martensite. The CPN surface appears dark because of the compound layer, Figure 4(c).

The cross-section microstructures of the samples are shown in Figure 5. A compound layer (CL) circa 15 μm thick grew on top of the CPN (530 ºC) specimen, while an adjacent nitrogen diffusion zone (DZ) circa 165 μm in thick was formed. It is important to point out that the nitrided case of the CPN specimens was strongly etched by Nital 4%, so the Compound Layer and the Diffusion Zone became severely darkened, as shown in Figure 5(a). The etching effect observed in the Diffusion Zone is a consequence of the precipitation of chromium nitrides, decreasing the nitrogen content in solid solution and compromising the passivation capacity of this region. Increasing the plasma nitriding temperature above 480 °C increases the volume fraction of precipitated iron and chromium nitrides [29-31]. Figure 5 clearly shows the harmful effect of the 530 °C conventional plasma nitriding on the corrosion resistance of the alloy, as will be shown later. For LTPN, an unetched layer, 50 μm in thick, can be seen. This nitrided layer mainly consists of expanded ferrite/martensite α$_N$/α'$_N$, Figure 5(b). Iron nitride intergranular and transgranular precipitates can also be seen, identified in the diffraction patterns as ε-Fe$_3$N and γ'-Fe$_4$N, shown in Figure 1. This result agrees with research works in the literature, reporting the formation of "expanded martensite" [32,33]
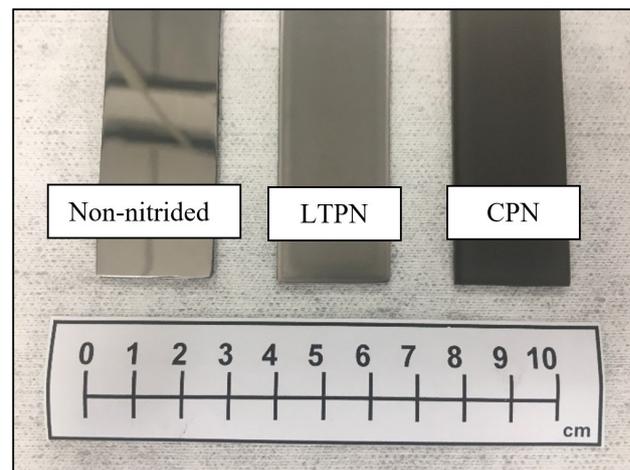

Figure 2. Microstructure of the as-received UNS S41003. Villela's reagent.

Figure 3. Surface finish of the non-nitrided sample (as polished) and after LTPN and CPN.
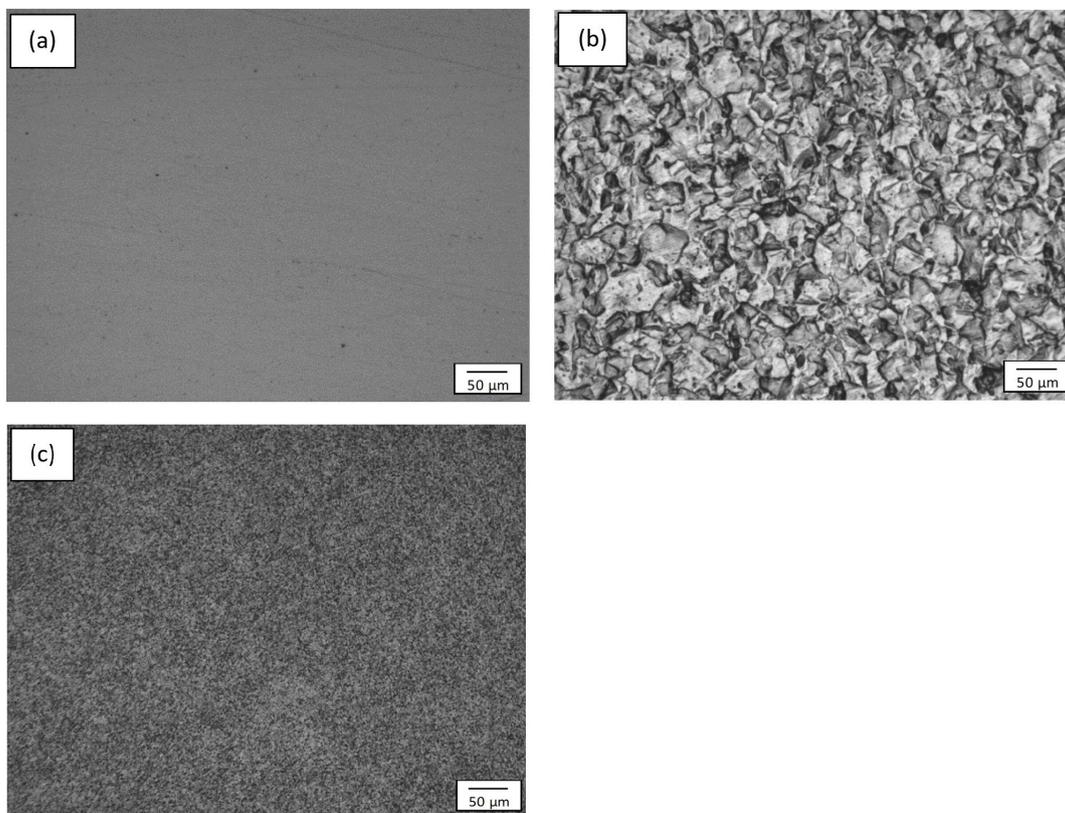
Figure 4. LOM images taken on top of (a) the as-polished sample, (b) after LTPN, and (c) CPN. Without etching.
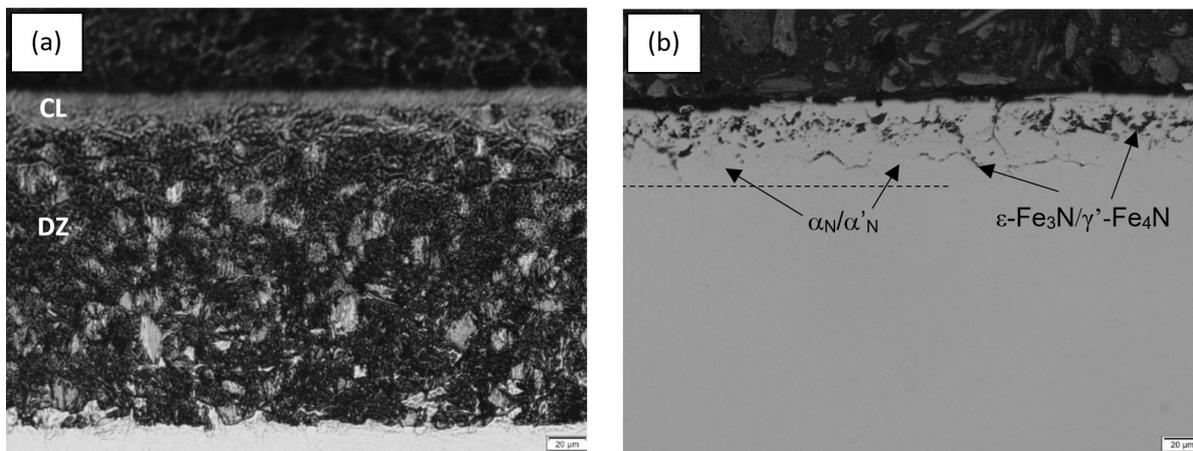

Figure 5. Microstructure of the cross-section of the nitrided cases: (a) after CPN and (b) after LTPN. Nital 4%.

or "expanded ferrite" [24,34], where interstitial nitrogen is present in the tetragonally distorted BCC ferrite lattice. Chromium depletion of the expanded phases matrix does not occur, as chromium nitride precipitation is suppressed due to the low substitutional diffusivity at the low plasma nitriding temperature. Iron nitrides and nitrogen supersaturated expanded phases do not impair the corrosion resistance of the nitrided Nital 4% etched case.

Figure 6 shows the surface microhardness measurements of the non-nitrided 410S steel, indicating 247 HV0.05 for the ferrite/martensite phases. The surface hardness of the LTPN was 1296 HV0.05, and the CPN was 1275 HV0.05. CPN and LTPN effectively increase surface hardness up to 4 times the surface hardness of the non-nitrided substrate. Surface hardening by nitriding is related to different mechanisms for LTPN and HTPN.
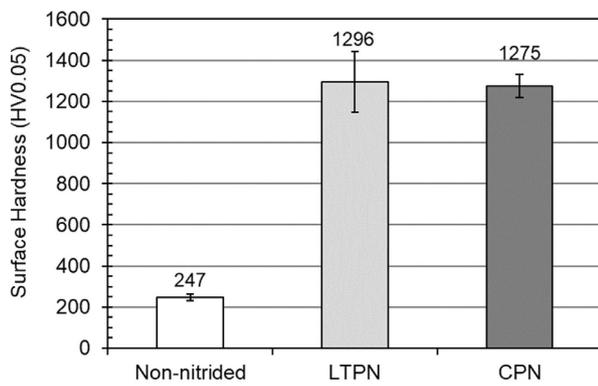
Figure 6. Surface hardness before and after plasma nitriding.

Figure 7. Transverse surface hardening for Conventional Plasma Nitriding and Low-Temperature Plasma Nitriding.

For the CPN-treated specimens, surface hardening occurs due to the compound layer formed on the surface and the precipitation of iron and chromium nitrides in the diffusion zone [35,36]. For the LTPN-treated specimens, hardening occurs due to interstitial nitrogen supersaturation of the crystalline lattice, distorting the expanded ferrite/martensite phases (α_N/α'_N) crystal lattices [23,37,38], with a minor contribution of coarser iron nitrides.

Transverse hardness profiles are shown in Figure 7. For conventional plasma nitriding (CPN), transverse hardening occurs with the formation of a maximum hardness plateau as a result of a fine and homogeneous coherent chromium nitride precipitation, as confirmed by XRD analysis. The formation of a maximum hardness plateau, which increases in depth with increasing nitriding temperature and exhibits a sharp decrease after the maximum hardness, is a significant characteristic of the transverse hardness profiles of high chromium steel in the CPN specimens [35,36]. Considering the nitride-forming substitutional element's strong interaction with nitrogen, the nitrided layer's growth kinetics and hardening are proportional to the nitrogen volume and grain boundaries diffusion. Strong interaction between N and Cr promotes the trapping of N atoms and nitride precipitation at the moving nitriding interface. As the Cr-N interaction is strong, the nitriding interface grows by a trapping-detrapping mechanism and assumes a planar growth interface, resulting in the observed upper shelf/lower shelf hardness profile with a steep gradient in between [39-41]. For the LTPN treatment, carried out at 400 °C, nitrogen diffusion in the matrix is the controlling mechanism, expanding the ferrite/martensite lattice. Little or no nitride precipitation affects diffusion kinetics. Hardening occurs by a solid solution mechanism, where the volume expansion of the BCC crystalline lattice increases hardness and generates residual compressive stresses [31-34]. Hardness is proportional to the nitrogen content dissolved in the expanded phase across the nitrided case resulting the observed diffuse shape.

Nanoindentation tests were performed on the specimens' top surface to determine the surface layers' mechanical properties. Figure 8 shows the load-displacement curves of non-nitrided and nitrided specimens. Table 2 shows the values
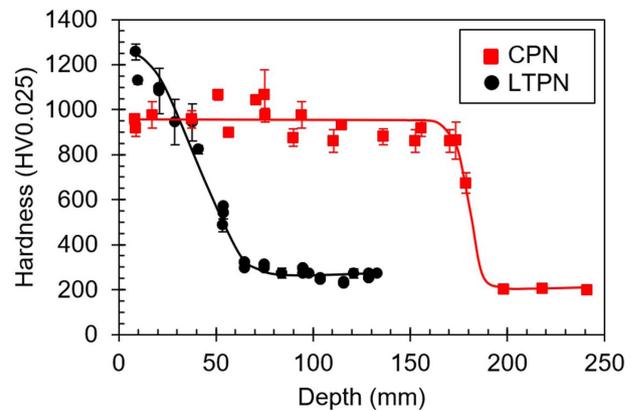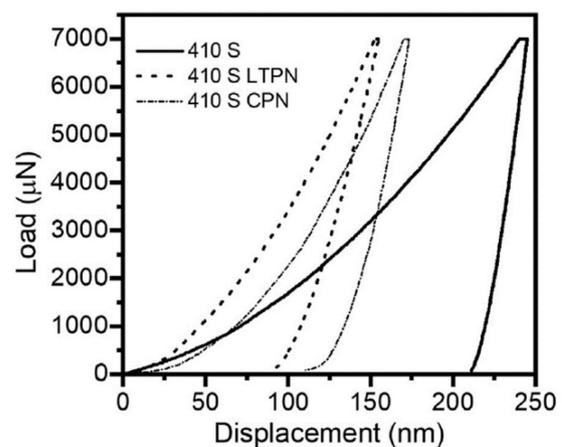

Figure 8. Load-displacement curves of non-nitrided and nitrided specimens obtained on nanoindentation tests.

of Hardness (H), Young modulus (E), H/E ratio, calculated elastic recovery (We), and calculated energy dissipation coefficient (Kd), of the non-nitrided and nitrided specimens. The surface hardness of the nitrided specimens is much higher than that of the non-nitrided specimens, which agrees with the microhardness results. Nitrided specimens have higher We and lower Kd values than the non-nitrided ones, suggesting that they are more resistant to plastic deformation, which is consistent with their higher hardness. Recco et al. [21] and Espitia et al. [23] observed that layers presenting a lower We and a higher Kd have a lower resistance to plastic deformation. The ratio H/E, related to the wear resistance, was also measured [42]. The nitrided specimens show a higher H/E ratio than the non-nitrided specimen, indicating enhanced wear resistance. Finally, one can see that the lowest Kd/We ratio is obtained for the LTPN specimen (see Table 2), indicating a better performance of the higher nitrogen content expanded martensite phase. Improvements in the elastic response of the nitrided layer have been reported by Espitia et al. [23] and Kamminga et al. [43].

Table 2. Hardness (H), Young modulus (E), H/E ratio, elastic recovery (We), and energy dissipation coefficient (Kd) of non-nitrided and nitrided specimens by depth sensing indentation with 7000 μN

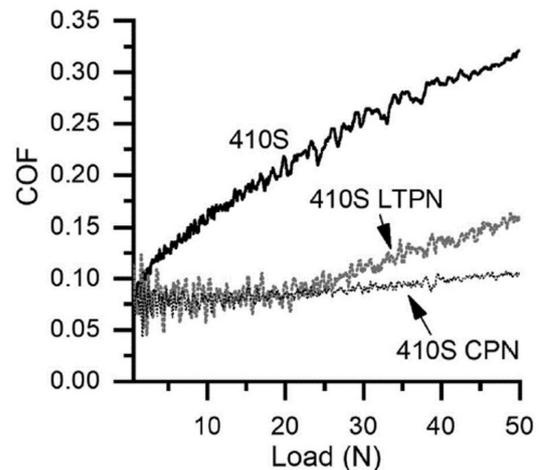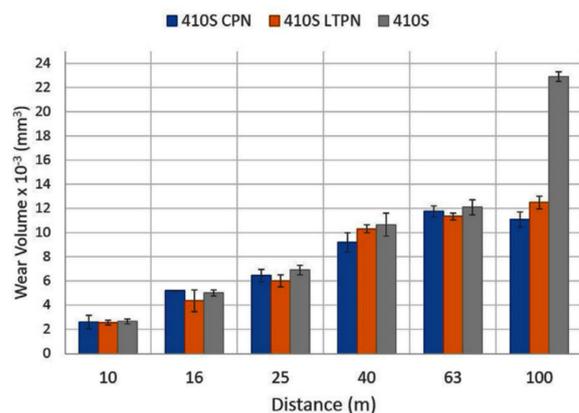| Specimen	H (GPa)	E (GPa)	H/E	We (%)	Kd (%)
Non-nitrided	4.4 + 0.5	202 + 7	0.02 + 0.002	14 + 1	84.5 + 0.9
CPN	9.1 + 1.0	211 + 25	0.04 + 0.005	36 + 2	63.3 + 3.4
LTPN	13.2 + 1.8	203 + 23	0.06 + 0.003	40 + 4	56,9 + 2.2

3.3 Micro-scratch and micro-abrasion wear tests

Figure 9 shows friction coefficients (COF) obtained in the scratch test for the nitrided and non-nitrided specimens. The nitrided samples submitted to the scratch test were not pre-polished. In the low-load case of the LTPN, the high deviation of the signal must be assigned to the surface roughness of the nitrided sample. Surface roughness is due to nitrogen diffusion generated during plasma nitriding, deforming the microstructure and creating a surface relief on the stainless steel surface due to the development of compressive residual stresses, as shown in Figure 4(b) [23]. Figure 9 shows that the COF is the greatest for the non-nitrided specimen and smaller for the nitrided specimens. For the non-nitrided specimen, no stability of the COF was observed, increasing up to a final value of 0.32.

In contrast, for the nitrided specimens, the COF is relatively constant, ~0.07, for loads below 23 N (corresponding to a 2.3 mm length track). At the beginning of the scratch test, the COF for both nitrided specimens was quite similar. However, COF values at the end of the test for the CPN specimen were smaller (~0.10) than those observed in the LTPN specimen (~0.15). Thick and hard layers provide better load-bearing capacities. The increased amount of nitrides can reduce adhesion and plastic deformation between surfaces in contact, resulting in lower coefficients of friction [44]. The constant COF behavior observed for the nitrided samples has been reported by Espitia et al. [23], and other authors [43-45] and is attributed to the occurrence of predominantly elastic deformation below 23 N.

On the other hand, when the extent of plastic deformation is great, and additionally, piling-up of material occurs in front of the indenter, the increase of COF can be even more intense. The track widths of the CPN and LTPN specimens, measured at the end of the scratch test (50 N), are 90 μm and 120 μm, respectively. Hoy et al. [46] showed that increasing the nitrided thickness reduces the width of the scratch tracks and increases the apparent scratch hardness, thus improving the load-bearing capacity of the nitrided layer. It is worth noting that this increase in the load-bearing capacity and greater amount of hard nitrides in the CPN specimen explain the slight COF reduction (0.10 max) compared to the (0.15 max.) obtained for the LTPN specimen.

Abrasion wear test results showed that plasma nitriding in the investigated temperature range could improve the wear resistance of ferritic-martensitic stainless steel. Figure 10 summarizes the wear volume results. The wear

Figure 9. Coefficient of friction versus applied load of plasma nitrided and non-nitrided samples.

Figure 10. Variation of wear volume as a function of the distance.

volume losses for both nitrided specimens, LTPN and CPN, were similar. The graph shows that significant differences between nitrided and non-nitrided specimens show up for a distance of 100 m, most probably due to hardness differences. Although the harder LTPN specimens do not present a compound layer, they lose almost the same wear volume shown by the CPN specimens, containing a compound layer formed by Fe_3N, Fe_4N, and CrN nitrides. Accordingly, the similar wear behaviors of LTPN and CPN specimens cannot be attributed to the presence of compound layers on the surface of both specimens. When the sliding distance increases, a transition between micro-rolling (mixed
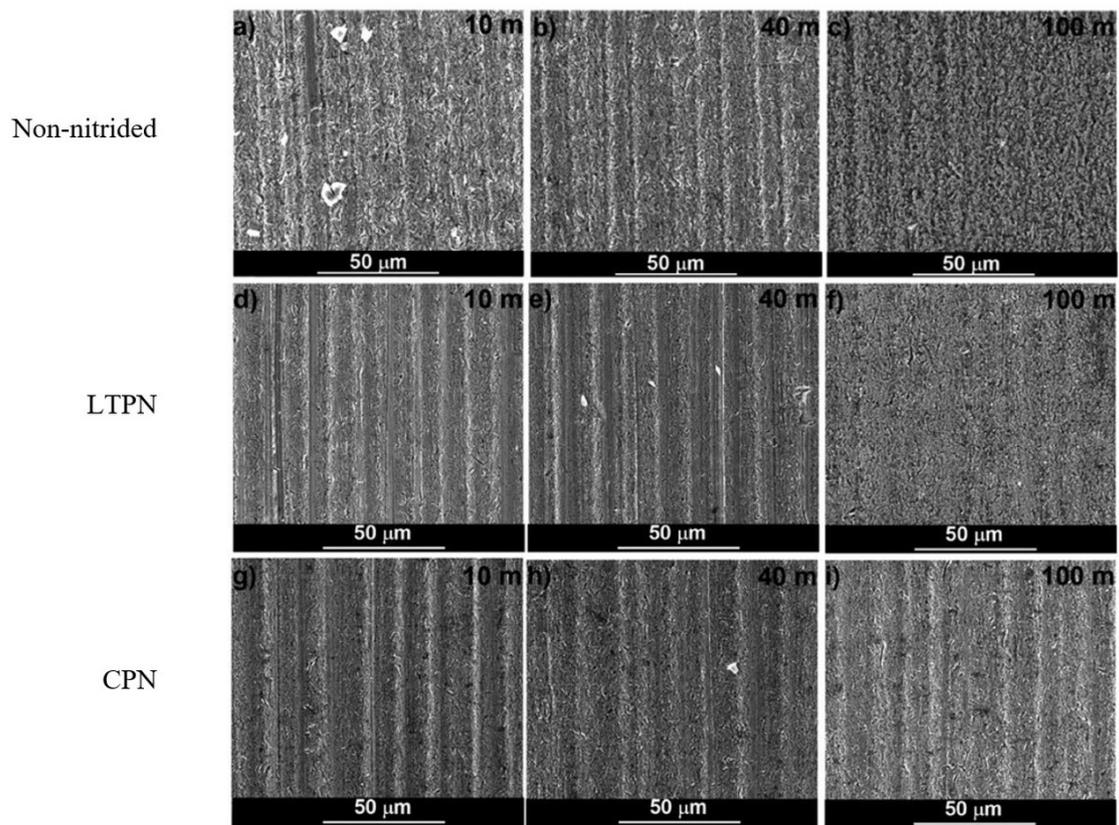
Figure 11. Wear scars inside microabrasion craters. 0.4 N applied load. Non-nitrided sample tested for a) 10 m, b) 40 m, and c) 100 m; LTPN sample tested for d) 10 m, e) 40m, and f) 100 m; CPN sample tested for g) 10 m, h) 40 m and i) 100 m.

grooving and rolling) abrasion to pure rolling abrasion can be observed for all conditions. For a constant load applied on the ball, smaller specific loads are applied to each particle, favoring the transition from grooving to rolling, as proposed by Trezona et al. [47] and Adachi and Hutchings [48]. A wear mechanism called by Cozza and Schon [49] micro-rolling abrasion can be seen, corresponding to the simultaneous action of rolling abrasion and grooving abrasion. Although the LTPN specimen exhibited better mechanical properties than the CPN specimen, similar abrasion resistances for both nitrided specimens can be attributed mainly to the higher case depth of the CPN specimen. The "micro-rolling abrasion" phenomenon occurs because abrasive particles roll along the grooves generated by grooving abrasion.

Figure 11 shows SEM images of the worn surface inside the ball craters for the non-nitrided, LTPN, and CPN-treated specimens after microabrasion carried out for 10, 40, and 100 m distances, under 0.4 N applied load. For all the specimens, mixed grooving and rolling wear marks indicate a transition from micro-rolling abrasion [49] to pure rolling abrasion. Trezona et al. [47] and Adachi and Hutchings [48] discuss the effects of changing the load applied to each abrasive particle during the microabrasion test, stating that the smaller the applied specific load, the greater the transition from grooving to rolling is. Although the results were obtained after testing under a constant applied load, one can see that the more wear-resistant the alloy, the lesser the transition from grooving to rolling is.

Although the above results were obtained after testing under a constant applied load, one can see that the more wear-resistant the surface, the lesser the transition from grooving to rolling is. Within the progress of the test, the accumulation of particles at the interface increases. It makes the load distributed in more particles at the interface, facilitating more particles to roll, as occurs in rolling abrasion [50].

3.4 Immersion tests in 3% $FeCl_3$ solution

The corrosion behavior of steel under immersion conditions is shown in Figure 12 [51]. Mass loss obtained by immersion tests in 3% $FeCl_3$ is shown in Figure 12a. The results show that LTPN did not deteriorate the corrosion resistance of 410S SS in the acidic water solution containing 3% $FeCl_3$, exhibiting similar behavior of the non-nitrided sample. Figure 12(b) shows that among the non-nitrided and the nitrided specimens, the CPN sample had the highest corrosion rate (554 mpy after 88 h). The corrosion behavior of the non-nitrided and nitrided samples was also confirmed by stereomicroscope image examination of the corroded surface morphologies, as shown in Figure 13. Figures 13(a) and 13(d)
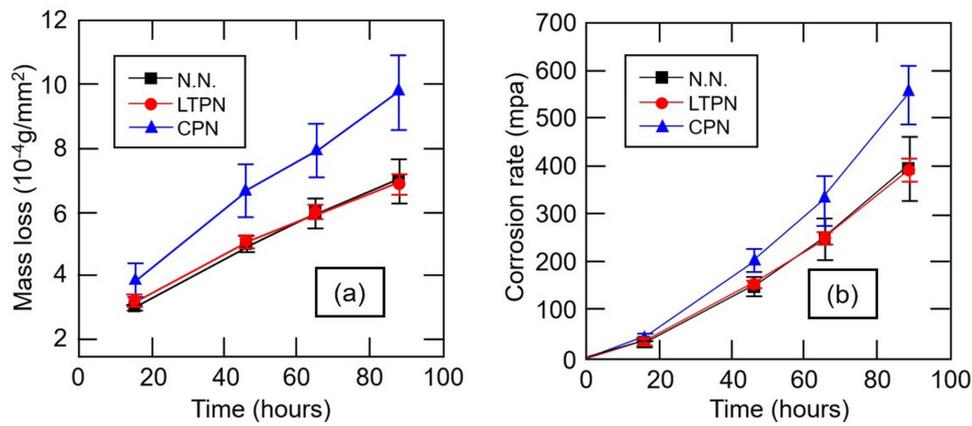
Figure 12. Corrosion mass loss (a) and corrosion rate (b) of non-nitrided (NN), LTPN, and CPN 410S SS specimens in a 3% $FeCl_3$ solution.
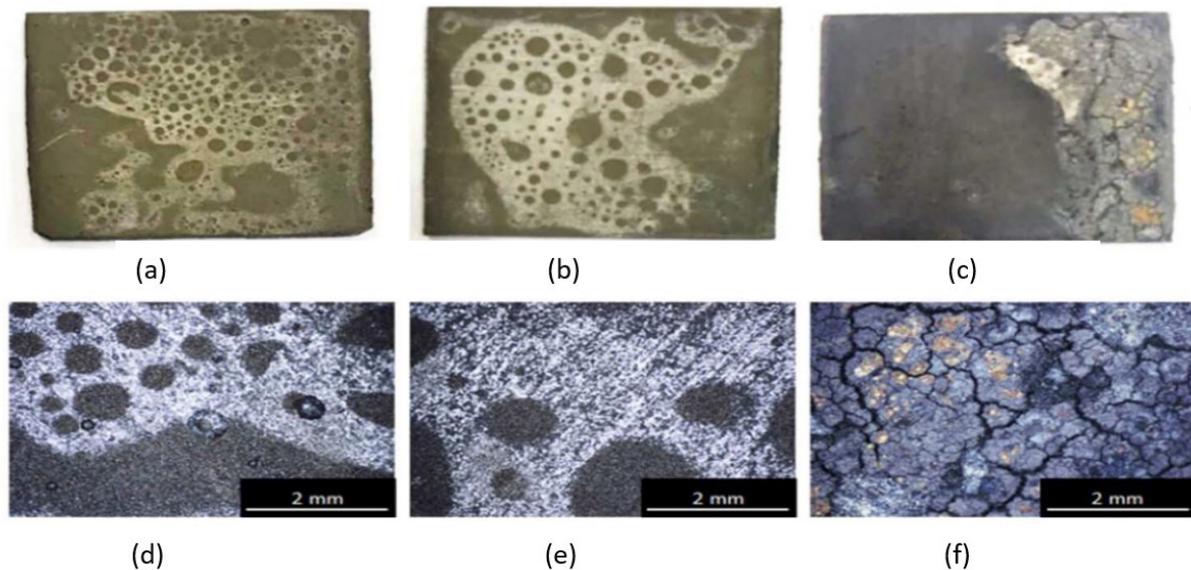

Figure 13. Stereo microscopy observations of specimens after immersion tests in a 3% $FeCl_3$ solution for 88 h of (a, d) untreated, (b, e) LTPN, and (c, f) CPN samples.

show the corroded surface of the untreated sample, where mild general corrosion is observed, with a few corrosion pits detected on the surface. For the LTPN specimen, the corrosion occurred as a general corrosion process, with no localized corrosion pits being observed, Figure 13(b) and 13(e). In contrast, the CPN sample was severely corroded and became rough after the immersion test, and the surface exhibited general corrosion with the release of corroded material, as shown in Figures 13(c) and 13(f). The same behavior was observed in previous work for martensitic stainless steel type 420 after LTPN at 380 ºC for 20 hours and immersion in an aqueous solution with 10% HCl for 120 hours [52].

The worst behavior shown by the CPN samples can be assigned to the corrosion/detachment of the ~15-µm thick compound layer after 15 h of the immersion test, exposing the α'_N and CrN precipitates existent in the diffusion nitrided

layer (details of the cross-section microstructure are previously reported in [53]. On the other hand, the LTPN-nitrided sample (400 °C) exhibited a homogeneous nitrided layer without CrN precipitates (see [53], which is in agreement with the immersion test in 3% $FeCl_3$ solution results.

4 Conclusions

1. Conventional Plasma Nitriding at 530 °C leads to a nitrided layer consisting of a 15 µm thick compound layer, followed by a diffusion zone with approximately 160 µm. The X-ray diffraction patterns confirm the intense precipitation of iron nitrides (ε-Fe_3N, γ'-Fe_4N) and chromium nitrides (CrN) in the diffusion zone

of the sample treated by the CPN process. In this condition, the surface is strongly etched by Nital, denoting its low corrosion resistance.

2. Low-temperature Plasma Nitriding leads to the formation of expanded metastable phases ferrite and martensite (α_N/α'_N), supersaturated in nitrogen. In this condition, the formation of a layer of compounds does not occur, the precipitation of ε-Fe_3N is incipient, and the precipitation of chromium nitride in the diffusion zone is suppressed. In the LTPN condition, the metallic matrix is not etched by Nital, denoting a better corrosion resistance.

3. After LTPN, the surface becomes opaque due to a surface relief effect generated by the formation of expanded ferrite/martensite grains without compromising the metallic appearance the stainless steel had before nitriding. After CPN, the surface becomes dark gray due to the formation of a rough compound layer.

4. After LTPN, the hardness profile varies with a diffuse gradient proportional to the nitrogen gradient towards the substrate. After CPN, the hardening profile shows upper and lower shelves, with a steep gradient in between. This profile is generated by the intense precipitation of nitrides and by a nitrogen trapping-detrapping mechanism associated with the precipitation of chromium nitrides.

5. Scratch test results indicate Friction Coefficients much smaller than the one observed for the non-nitrided specimen. The increase in the load-bearing capacity and greater amount of hard nitrides in the CPN specimen explain the slight COF reduction (0.10 max) compared to the (0.15 max.) obtained for the LTPN specimen.

6. Abrasion wear test results showed that plasma nitriding in the investigated temperature range could improve the wear resistance of ferritic-martensitic stainless steel. The wear volume losses for both nitrided specimens, LTPN and CPN, were similar. Similar microabrasion resistances were observed for both nitrided specimens, despite the LTPN specimen exhibiting better mechanical properties than the CPN specimen. This behavior can be attributed to the higher case depth of the CPN specimen.

7. Mixed grooving and rolling wear marks were observed inside wear craters, indicating a transition from micro-rolling abrasion to pure rolling abrasion. The more wear-resistant LTPN and CPN specimens showed a smaller trend to transition from grooving to rolling abrasion.

8. Corrosion resistance after LTPN is similar to that verified for the non-nitrided state, showing that the absence of precipitation of chromium nitrides, together with the increase in the nitrogen content in the layer, are efficient in achieving a hardening, about 5x the initial value without compromising the corrosion resistance.

References

1 Larisch B, Brusky U, Spies H-J. Plasma nitriding of stainless steels at low temperatures. Surface and Coatings Technology. 1999;116–119:205-211.

2 Czerwiec T, Renevier N, Michel H. Low-temperature plasma-assisted nitriding. Surface and Coatings Technology. 2000;131:267-277.

3 Venkatesan K, Subramanian C, Green LK. Influence of chromium content on corrosion of plasma-nitrided steels. Corrosion. 1997;53:507-515.

4 Wang L, Xu X, Yu Z, Hei Z. Low pressure plasma arc source ion nitriding of austenitic stainless steel. Surface and Coatings Technology. 2000;124:93-96.

5 Fewell M, Mitchell D, Priest J, Short K, Collins G. The nature of expanded austenite. Surface and Coatings Technology. 2000;131:300-306.

6 Christiansen T, Somers MAJ. Controlled dissolution of colossal quantities of nitrogen in stainless steel. Metallurgical and Materials Transactions. A, Physical Metallurgy and Materials Science. 2006;37:675-682.

7 Mingolo N, Tschiptschin AP, Pinedo CE. On the formation of expanded austenite during plasma nitriding of an AISI 316L austenitic stainless steel. Surface and Coatings Technology. 2006;201:4215-4218.

8 Bell T. Current status of supersaturated surface engineered S-phase materials. Key Engineering Materials. 2008;373-374:289-295.

9 Dong H. S-phase surface engineering of Fe-Cr, Co-Cr and Ni-Cr alloys. International Materials Reviews. 2010;55:65-98.

10 Kim S, Yoo J, Priest J, Fewell M. Characteristics of martensitic stainless steel nitrided in a low-pressure RF plasma. Surface and Coatings Technology. 2003;163-164:380-385.

11 Xi Y-T, Liu D-X, Han D. Improvement of corrosion and wear resistances of AISI 420 martensitic stainless steel using plasma nitriding at low temperature. Surface and Coatings Technology. 2008;202:2577-2583.

12. Xi Y, Liu D, Han D, Han ZF. Improvement of mechanical properties of martensitic stainless steel by plasma nitriding at low temperature. Acta Metall Sin. 2008;21:21-29.

13 Pinedo CE, Magnabosco R. Mecanismos de nitretação sob plasma do aço inoxidável martensítico AISI 420 nitretado a alta e baixa temperatura. Tecnologica em Metalurgia, Materiais e Mineração. 2015;12:257-264.

14 Pinedo CE, Larrotta SIV, Nishikawa AS, Dong H, Li X-Y, Magnabosco R, et al. Low temperature active screen plasma nitriding of 17-4 PH stainless steel. Surface and Coatings Technology. 2016;308:189-194.

15 Chiu LH, Su YY, Chen FS, Chang H. Microstructure and properties of active screen plasma nitrided duplex stainless steel. Materials and Manufacturing Processes. 2010;25:316-323.

16 Nagatsuka K, Nishimoto A, Akamatsu K. Surface hardening of duplex stainless steel by low temperature active screen plasma nitriding. Surface and Coatings Technology. 2010;205:S295-S299.

17 Sousa RRM, Araújo FO, Costa JAP, Oliveira AM, Melo MS, Alves C Jr. Cathodic cage nitriding of AISI 409 ferritic stainless steel with the addition of CH4. Materials Research. 2012;15:260-265.

18 Pinedo CE, Varela LB, Tschiptschin AP. Low-temperature plasma nitriding of AISI F51 duplex stainless steel. Surface and Coatings Technology. 2013;232:839-843.

19 Christiansen T, Somers MAJ. Decomposition kinetics of expanded austenite with high nitrogen contents. Z. Met. 2006;97:79-88.

20 Oliver WC, Pharr GM. An improved technique for determining hardness and elastic modulus using load and displacement sensing indentation experiments. Journal of Materials Research. 1992;7:1564-1583.

21 Recco AAC, Viáfara CC, Sinatora A, Tschiptschin AP. Energy dissipation in depth-sensing indentation as a characteristic of the nanoscratch behavior of coatings. Wear. 2009;267:1146-1152.

22 Câmara Cozza R, Rodrigues LC, Geraldo Schön C. Analysis of the micro-abrasive wear behavior of an iron aluminide alloy under ambient and high-temperature conditions. Wear. 2015;330–331:250-260.

23 Espitia LA, Dong H, Li XY, Pinedo CE, Tschiptschin AP. Scratch test of active screen low-temperature plasma nitrided AISI 410 martensitic stainless steel. Wear. 2017;376–377:30-36.

24 Tschiptschin AP, Varela LB, Pinedo CE, Li XY, Dong H. Development and microstructure characterization of single and duplex nitriding of UNS S31803 duplex stainless steel. Surface and Coatings Technology. 2017;327:83-92.

25 Pinedo CE, Varela LB, Tschiptschin AP. Low-temperature plasma nitriding of AISI F51 duplex stainless steel. Surface and Coatings Technology. 2013;232:839-843.

26 Kim SK, Yoo JS, Priest JM, Fewell MP. Characteristics of martensitic stainless steel nitriding a low-pressure RF plasma. Surface and Coatings Technology. 2003;163–164:380-385.

27 Christiansen TL, Somers MAJ. Stress and composition of carbon stabilized expanded austenite on stainless steel. Metallurgical and Materials Transactions. A, Physical Metallurgy and Materials Science. 2009;40:1791-1798.

28 Cheng L. Phase transformations in iron-based interstitial martensites [thesis]: Delft University; 1990. https://repository.tudelft.nl/islandora/object/uuid:bbe1aa0b-a680-4d94-9ec9-b7ed33200b6e?collection=research

29 Li Y, He Y, Xiu JJ, Wang W, Zhu YJ, Hu B. Wear and corrosion properties of AISI 420 martensitic stainless steel treated by active screen plasma nitriding. Surface and Coatings Technology. 2017;329:184-192.

30 Pinedo CE, Monteiro WA. Characterization of plasma nitrided case on martensitic stainless steel by scanning electron microscopy. Acta Microscópica. 2001;1:315-316.

31 Sousa RRM, Araújo FO, Costa JAP, Oliveira AM, Melo MS, Alves C Jr. Cathodic cage nitriding of AISI 409 ferritic stainless steel with the addition of CH4. Materials Research. 2012;15:260-265.

32 Espitia LA, Varela L, Pinedo CE, Tschiptschin AP. Cavitation erosion resistance of low temperature plasma nitrided martensitic stainless steel. Wear. 2013;301:449-456.

33 Pinedo CE, Larrotta SIV, Nishikawa AS, Dong H, Li XY, Magnabosco R et al. Low temperature active screen plasma nitriding of 17–4 PH stainless steel. Surface and Coatings Technology. 2016;308:189-194.

34 Tuckart W, Gregorio M, Iurman L. Sliding wear of plasma nitrided AISI 405 ferritic stainless steel. Surface Engineering. 2010;26:185-190.

35 Pinedo CE, Monteiro WA. Surface hardening by plasma nitriding on high chromium alloy steel. Journal of Materials Science Letters. 2001;20:147-149.

36 Pinedo CE, Monteiro WA. On the kinetics of plasma nitriding a martensitic stainless steel Type AISI 420. Surface and Coatings Technology. 2004;179:119-123.

37 Pinedo CE. Nitretação por plasma de aços inoxidáveis. Metals and Materials. 2002;60:162-164.

38 Espitia LA, Dong H, Li XY. Cavitation erosion resistance and wear mechanisms of active screen low temperature plasma nitrided AISI 410 martensitic stainless steel. Wear. 2015;332-333:1070-1079.

39 Jack DH. Nitriding. In: Iron and Steel Institute, editor. Heat Treatment'73. London: The Metal Society; 1973. p. 39-50.

40 Lightfoot J, Jack DH. Kinetics of nitriding with and without compound layer formation. In: Iron and Steel Institute, editor. Heat Treatment'73. London: The Metal Society; 1973. p. 59-65.

41 Pinedo CE, Monteiro WA. Influence of heat treatment and plasma nitriding parameters on hardening an AISI 420 martensitic stainless steel. In: Proceedings of the 18th International Federation for Heat treatment and Surface Engineering. Rio de Janeiro. Switzerland: IFHTSE 2010. p. 4750-4757.

42 Leyland A, Matthews A. On the significance of the H/E ratio in wear control: a nanocomposite coating approach to optimised tribological behaviour. Wear. 2000;246:1-11.

43 Kamminga JD, Alkemade PFA, Janssen GCAM. Scratch test analysis of coated and uncoated nitrided steel. Surface and Coatings Technology. 2004;177–178:284-288.

44 Rovani AC, Breganon R, Souza GS, Brunatto SF, Pintaúde G. Scratch resistance of low-temperature plasma nitrided and carburized martensitic stainless steel. Wear. 2017;376–377:70-76.

45 Subhash G, Zhang W. Investigation of the overall friction coefficient in single-pass scratch test. Wear. 2002;252:123-134.

46 Hoy R, Kamminga JD, Janssen GCAM. Scratch resistance of CrN coatings on nitrided steel. Surface and Coatings Technology. 2006;200:3856-3860.

47 Trezona RI, Allsopp DN, Hutchings IM. Transition between two-body and three body abrasive wear: influence of test conditions in the microscale abrasive wear test. Wear. 1999;225–229:205-214.

48 Adachi K, Hutchings IM. Wear-mode mapping for the micro-scale abrasion test. Wear. 2003;255:23-29.

49 Cozza RC, Schon CG. Evidence of superposition between grooving abrasion and rolling abrasion. Tribology Transactions. 2015;58:875-881.

50 Calderon CDR, Cabrera LIF, Ramíres IC. A novel tester to examine micro-abrasion of materials in oscillating sliding contact – The case study of a total knee replacement biomaterial. Wear. 2021;476:203661.

51 Varela LB, Umemura MT, Calderón-Hernández JW, Pinedo CE, Kolawole FO, Tschiptschin AP. Corrosion resistance of low-temperature and conventional plasma-citrided 410S ferritic-martensitic stainless steels. Materials Performance and Characterization. 2021;10(1):181-188.

52 Tschiptschin AP, Pinedo CE. Surface hardening of stainless steel. In: Singh A, editor. Stainless steels. London: IntechOpen; 2022. p. 65-96.

53 Umemura MT, Varela LB, Pinedo CE, Cozza RC, Tschiptschin AP. Assessment of tribological properties of plasma nitrided 410S ferritic-martensitic stainless steels. Wear. 2019;426-427:49-58.